



## Shear deformation of dry polycrystalline olivine under deep upper mantle conditions using a rotational Drickamer apparatus (RDA)

Takaaki Kawazoe\*, Shun-ichiro Karato, Kazuhiko Otsuka, Zhicheng Jing, Mainak Mookherjee<sup>1</sup>

Department of Geology and Geophysics, Yale University, 210 Whitney Avenue, New Haven, CT 06511, USA

### ARTICLE INFO

#### Article history:

Received 3 December 2007

Received in revised form 4 June 2008

Accepted 30 June 2008

#### Keywords:

Olivine  
Viscosity  
Rheology  
Mantle dynamics  
Mantle convection  
Upper mantle  
Pressure

### ABSTRACT

Shear deformation experiments on dry hot-pressed polycrystalline San Carlos olivine have been conducted at 4.9–9.6 GPa, 1300–1870 K and strain rates of  $0.6\text{--}7.4 \times 10^{-5} \text{ s}^{-1}$  using a rotational Drickamer apparatus (RDA) at a synchrotron facility. The stress was measured from the orientational dependence of lattice spacing for the (130), (131), (112), (122), (140) and (241) planes, as well as from the dislocation densities. Based on the mechanical and microstructural observations, we infer that deformation occurs by power-law creep involving dislocation glide and climb under high temperature conditions, whereas deformation is due to exponential creep through the Peierls mechanism at relatively low temperatures. In both regimes the strength of olivine at steady-state deformation at these pressures is much larger than those at lower pressures. The activation volumes  $V^*$  is estimated to be  $\sim 15\text{--}20 \times 10^{-6} \text{ m}^3/\text{mol}$  for the power-law creep. Combined with the previous results under wet conditions, we present the recommended values of flow law parameters on olivine for power-law creep constrained by high-pressure deformation experiments.

© 2008 Elsevier B.V. All rights reserved.

### 1. Introduction

Influence of confining pressure on plastic deformation is large and complicated (e.g., Chapter 10 of Karato, 2008). For example, the strain-rate for a given stress can change as much as  $\sim 10$  order of magnitude by pressure in the upper mantle. Consequently, precise knowledge of pressure dependence of high-temperature creep is critical for understanding the geodynamics of Earth's interior.

However, due to the difficulties in quantitative experimental studies of plastic deformation at high-pressures and temperatures, the influence of the pressure on the creep strength of olivine remains controversial although many experimental studies have been performed on olivine deformation. In many cases, the pressure effect on the creep strength is evaluated as the activation volume  $V^*$  (e.g., Karato, 2008). The reported activation volumes for dislocation creep in dry olivine range from 0 (Li et al., 2006) to  $27 \times 10^{-6} \text{ m}^3/\text{mol}$  (Green and Borch, 1987). This range of activation volume would cause a variation of viscosity difference by  $\sim 10$  orders of magnitude at the deep upper mantle conditions. A large discrepancy in the reported values of activation volume is due to

the difficulties in obtaining quantitative data on high-temperature creep above 3 GPa at high temperatures.

This situation is changing due to the development of new types of deformation apparatus such as a rotational Drickamer apparatus (RDA; Xu et al., 2005; Yamazaki and Karato, 2001) and deformation-DIA (D-DIA; Wang et al., 2003). When used with a synchrotron X-ray facility, these new apparatuses allow us to conduct quantitative studies of plastic deformation to 16 GPa (RDA) and to 10 GPa (D-DIA), respectively. In particular, there have been a large number of publications on olivine rheology using the D-DIA (Li et al., 2003, 2004, 2006; Raterron et al., 2004, 2007). Despite substantial technical developments, new results reported above have amplified the discrepancy among various studies rather than to improve our understanding of deep mantle rheology. This motivated us to explore the influence of pressure on high-temperature dislocation creep in olivine using RDA. Compression geometry of RDA makes quantitative deformation experiments more complicated for RDA than for D-DIA due to existence of uniaxial stress during shear deformation. However, as we will show in this paper, with the improvements on cell assembly, it is possible to obtain quantitative rheological data from RDA that place strong constraints on the influence of pressure on rheological properties.

The purpose of this paper is to report the recent results on olivine deformation using RDA. In order to assess the extent to which we can use the present results to constrain deep upper mantle rheology, we will describe a number of technical developments in

\* Corresponding author. Tel.: +1 203 432 5791; fax: +1 203 432 3134.

E-mail address: [takaaki.kawazoe@yale.edu](mailto:takaaki.kawazoe@yale.edu) (T. Kawazoe).

<sup>1</sup> Now at Bayerisches Geoinstitut, Universität Bayreuth, D-95440 Bayreuth, Germany.

the cell assembly including the estimation and characterization of temperature distributions in a sample.

As we will emphasize in this paper, several issues need to be addressed in order to obtain results that can be applied to investigate the deep mantle rheology (see also Karato, 2008). They include sample characterization (water content and grain-size), steady-state versus transient creep and the flow law regime (power-law versus exponential flow law). If all of these issues are appropriately addressed, we can obtain results that can be interpreted in a physically plausible model and can be applied to Earth's interior, although there are remaining technical issues in the stress measurements using X-ray diffraction.

**2. Experimental and analytical methods**

**2.1. Starting material**

Hot-pressed polycrystalline San Carlos olivine was used as a starting material. Single crystals of San Carlos olivine with no inclusions were hand-picked, ground and sorted in the distilled water. The sorted San Carlos olivine powder with grain size of 2–3 μm was mixed with 1–2 wt% San Carlos orthopyroxene to control the activities of oxide components in the olivine. The mixture was hot-pressed at 3 GPa and 1370 K for 2 h without additional water using a Kawai apparatus. The water content of the starting hot-pressed material was determined by the Fourier-transform infrared (FT-IR) spectroscopy (Fig. 1) and is ranged from 1100 to 2800 H/10<sup>6</sup> Si (using the Paterson calibration, described later). The hot-pressed sample is annealed at high-pressure and temperature before deformation. The microstructure (including grain-size) and the water content of samples after annealing and after deformation experiments were also studied as we report in the later part of this paper.

**2.2. Experimental procedure**

Deformation experiments have been conducted at *P* (confining pressure) = 4.9–9.6 GPa, *T* (temperature) = 1300–1870 K and  $\dot{\epsilon}$  (strain-rate) = 0.6–7.4 × 10<sup>-5</sup> s<sup>-1</sup> using the RDA at X17B2 beam-line, National Synchrotron Light Source (NSLS), Brookhaven National Laboratory (BNL), USA. The sample geometry and the cross-section

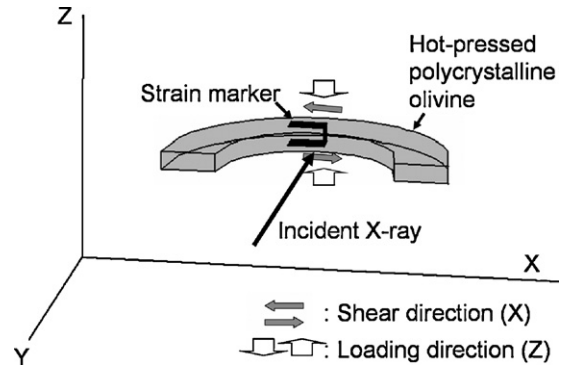


**Fig. 2.** Sample geometry. Z is the direction of the loading. Y is the direction of X-ray beam and is normal to Z. X-direction is perpendicular to both of them and parallel to the shear direction. Strain marker is placed as shown in this figure in order to measure shear and uni-axial strain rate.

of a typical cell assembly are shown in Figs. 2 and 3, respectively. Attention has been paid to several issues in the development of the cell assembly. First, because torsion tests are conducted in which stress and strain in a sample change with the distance from the rotational axis, we use a ring or a half-ring shape sample to minimize the variation in stress (and strain-rate) within a sample. The typical sample dimension is 1.6 mm (inner diameter) and 2.4 mm (outer diameter), and thickness is 40–50 μm. With this current sample geometry, the variation in strain rate and stress in a sample is 30% and 8%, respectively (we assume the stress exponent of *n* = 3.5). Second, in order to minimize the extrusion that occurs due to compression, a sample is surrounded by a strong material (Al<sub>2</sub>O<sub>3</sub>). Third, in order to minimize the absorption of X-ray along the path, a large portion of gasket (pyrophyllite) is replaced with a polyetheretherketone (PEEK) polymer and boron-epoxy. Fourth, a molybdenum strain marker was placed in the sample as shown in Figs. 2 and 3 to determine both shear and uni-axial strain and their rates.

The sample was heated using internal disk heaters made of a hot-pressed TiC-diamond composite. Temperature in the sample was measured by a thermocouple (Pt–Pt<sub>90</sub>Rh<sub>10</sub>) in a few static experiments, but a thermocouple was not used in most of the deformation experiments because of the difficulties in avoiding short-circuit during large-strain shear. However, by a combination of a limited thermocouple measurements and also some temperature measurements using an enstatite-diopside geothermometry (Gasparik, 1996), we have established a relationship between the

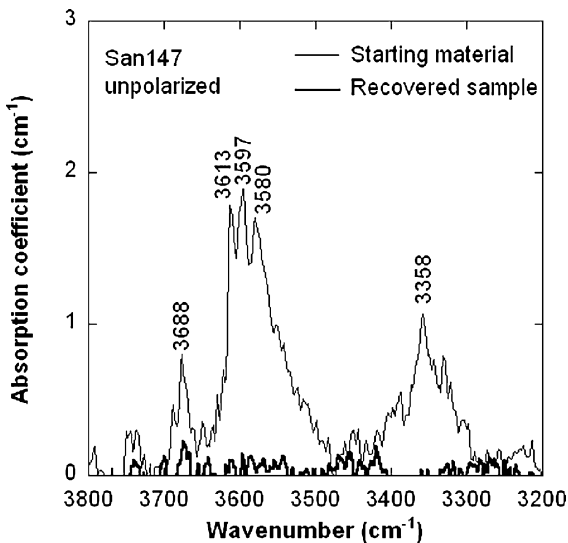


**Fig. 1.** Unpolarized FT-IR spectra of a recovered sample and a starting material of run #San147-3. Bold and thin lines are spectra of the recovered sample and the starting material, respectively. These spectra yield the water contents of the recovered sample and the starting material as less than 50 and 1100 H/10<sup>6</sup> Si, respectively.

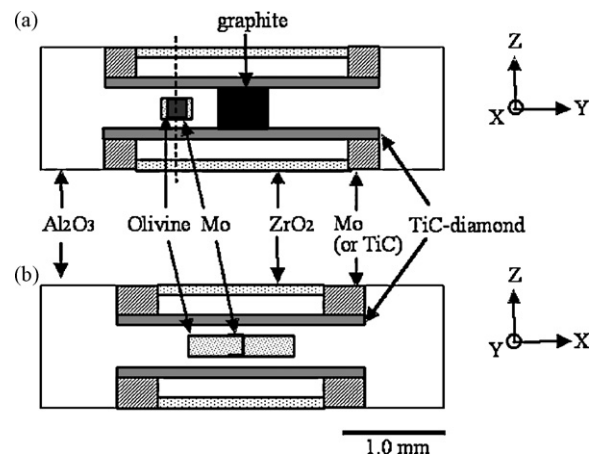


**Fig. 3.** Cross-section of the cell assembly used in run #San147. (a) A cross-section in the Y–Z plane (cut in the center). (b) A cross-section in X–Z plane (cut in the plane shown by a broken line in (a)).

power and cell thickness and sample temperature. We use this empirical relationship to estimate the average temperature during deformation or annealing experiments using the observed power and cell thickness. The uncertainties in temperature originate from (i) temperature gradient in a sample and (ii) the uncertainties in the power, thickness versus sample temperature calibration. The temperature gradient in the sample was also determined using the enstatite-diopside geothermometry and it is less than  $\pm 60$  K. The uncertainties in the temperature calibration as a function of power and sample thickness is  $\pm 50$  K. Considering these uncertainties, we estimate the uncertainty in temperature estimate in this study is  $\sim \pm 85$  K.

The samples were compressed to desired loads (pressures) at room temperature and then annealed at high temperatures for 30–60 min before deformation to reduce the density of dislocations that were generated during pressurization. The electric power to the heater was kept constant during annealing and deformation. Temperature during annealing is higher by 30–200 K than that at steady-state deformation because the cell thickness during annealing was thicker than that during steady-state deformation. Annealing is critical because a number of defects (dislocations and fine grains) are created during the pressurization processes in RDA. The necessary annealing conditions were explored based on off-line experiments in which grain-size, grain-boundary morphology and dislocation density after annealing were studied. The grain-boundary morphology shows near equilibrium geometry (Fig. 4). Reduction of the sample stress (to less than  $\sim 1/3$  of the steady-state value) after annealing was also confirmed using in situ X-ray

observation which is described later. After annealing, shear traction was applied to the samples under high pressure and temperature by rotating one of the WC anvils.

During deformation, deviatoric stress and strain rate in the samples were measured by means of in situ X-ray diffraction and radiography, respectively. Energy-dispersive X-ray diffraction patterns were taken using an optical system composed of an incident slit, a conical receiving slit and a multi-element solid-state detector. White incident X-rays were collimated by a  $50 \mu\text{m} \times 50 \mu\text{m}$  or a  $100 \mu\text{m} \times 100 \mu\text{m}$  slit and the height of a conical receiving slit was  $50 \mu\text{m}$ . Diffracted X-rays were taken at four different azimuth angles of  $0^\circ$ ,  $30^\circ$ ,  $60^\circ$  and  $90^\circ$  for typically 15 min. Using  $\text{Al}_2\text{O}_3$  powder as a standard material,  $2\theta$  angles for the four elements were determined and ranged from  $6.480^\circ$  to  $6.585^\circ$  that depends on each detector and run with an error of  $\pm 0.001$ – $0.003^\circ$  for each detector for a given run. Stress values were calculated from the observed azimuth dependence of d-spacings of olivine peaks, (1 3 0), (1 3 1), (1 1 2), (1 2 2), (1 4 0) and (2 4 1). X-ray radiograph of the strain marker was taken using a YAG crystal and a CCD camera. Detailed description of the in situ measurements of stress and strain at the X17B2 beam-line can be found elsewhere (Chen et al., 2004). With our diffraction geometry, the volume from which diffracted X-ray is collected to the detector has an elongated shape (Xu et al., 2005) and the stress values are the average stress from a sample region ranging from the inner to the outer part. Since a sample is deformed by torsion, stress will change from the inner to the outer region of a sample. With the ring-shaped sample, the variation in stress in a sample is  $\sim 8\%$  for the stress exponent of  $n = 3.5$ .

We used a model of stress versus lattice strain relationship developed by Singh (1993) with a modification to a more general stress geometry that includes both uni-axial compression and simple shear (Xu et al., 2005),

$$d_{hkl} = d_{hkl}^0 \left[ 1 + \frac{\sigma_U}{6G}(1 - 3 \cos^2 \psi) - \frac{\sigma_S}{2G} \sin \psi \cos \psi \right] \quad (1)$$

where  $d_{hkl}$  is the d-spacing measured as a function of azimuth angle  $\psi$ ,  $d_{hkl}^0$  is the d-spacing under the hydrostatic pressure,  $G$  is the shear modulus,  $\sigma_U$  is the uni-axial stress,  $\sigma_S$  is the deviatoric stress, defined by

$$\sigma_{ij} = \begin{bmatrix} -\frac{\sigma_U}{3} & 0 & \frac{\sigma_S}{2} \\ 0 & -\frac{\sigma_U}{3} & 0 \\ \frac{\sigma_S}{2} & 0 & \frac{2\sigma_U}{3} \end{bmatrix} \quad (2)$$

where the Z direction is parallel to the loading direction and the X-direction is parallel to the shear direction (Figs. 2 and 3). We adopt the shear modulus of polycrystalline San Carlos olivine determined by ultrasonic measurements at high pressure and temperature (Liu et al., 2005) and it is close to an average between shear modulus under Reuss (iso-stress) and Voigt (iso-strain) conditions (errors caused by using an average elastic modulus,  $\sim 10\%$ ) are small compared to the variation in stress levels (by a factor of  $\sim 3$ ) determined by different  $(hkl)$  caused by plastic anisotropy). The stresses and  $d_{hkl}^0$  were determined to fit observed  $d_{hkl}$  to Eq. (1) using the least-squares method. Peak position and its uncertainty were determined by using a PeakFit software (SeaSolve Software Inc.) and the error represents one standard deviation. Uncertainty of the peak position was propagated to that of the stress using Eq. (1).

We note that Singh (1993)'s model does not include the influence of plastic anisotropy in controlling stress distribution that causes a large uncertainty in the stress measurement (e.g., Weidner et al., 2004). In order to provide additional constraints, stress in the samples was also determined using a relationship between the stress and dislocation density (Karato and Jung, 2003). Pressure

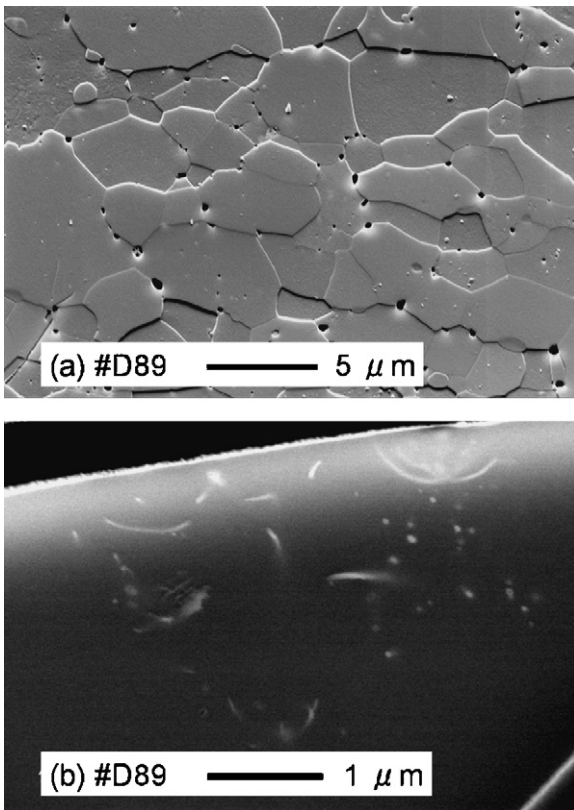


**Fig. 4.** Microstructures of annealed sample at 10 GPa and 1960 K for 60 min (run #D89). (a) SEI of the sample etched by 35%  $\text{HNO}_3$ . The sample was sectioned in X–Z plane. Average grain-size is  $6.3 \mu\text{m}$  and grain-boundary morphology suggests nearly equilibrium morphology. Most grains are elongated to X direction due to initial compression. (b) BSEI of the sample decorated at 1103 K in air. Dislocations can be observed as white lines or dots. The X direction is horizontal in these figures.

effect on the dislocation density–stress relationship is corrected using that on shear modulus of polycrystalline San Carlos olivine (Liu et al., 2005) because pressure conditions of this study were higher than that where the relationship was calibrated (0.3 GPa). The resolution and limitations of this technique are discussed by Karato and Jung (2003). The error in stress estimate from this technique is ~10–15% that is better than the uncertainties in stress estimate by the X-ray radial diffraction caused by the discrepancies in stress estimated from diffraction by different lattice planes. Pressure was calculated using the equation of state of San Carlos olivine (Liu and Li, 2006). The unit cell volume was calculated using the  $d_{hkl}^0$ . Uncertainty of the pressure originates from that of the unit cell volume and its variation during deformation.

Strains and strain-rates in both shear and uni-axial directions were measured by the X-ray radiographs of the strain marker and calculated using the following equations, respectively:

$$\dot{\epsilon}_S = \frac{1}{2h} \frac{\partial w}{\partial t} \quad (3)$$

and

$$\dot{\epsilon}_U = -\frac{1}{h} \frac{\partial h}{\partial t} \quad (4)$$

where  $\dot{\epsilon}_S$  and  $\dot{\epsilon}_U$  are the shear and uni-axial strain rates, respectively,  $w$  is the displacement in shear direction,  $h$  is the height of the sample and  $t$  is the time. The  $\dot{\epsilon}_S$  changes with the distance from the rotational axis because torsion tests were conducted in this study. Inner and outer radii from the centre (rotational axis) in the recovered sample were 0.75–0.81 and 1.19–1.25 mm, respectively. This difference caused the difference of the  $\dot{\epsilon}_S$  between inner and outer parts of the samples as less than  $\pm 30\%$ . On the other hand, uncertainties of  $w$  and  $h$  were  $\pm 0.3$  and  $\pm 3 \mu\text{m}$ , respectively, and these uncertainties results in that of  $\dot{\epsilon}_S$  as less than  $\pm 20\%$ .

In principle, results from the RDA can be analysed for shear and compressional deformation separately, but considering the large uncertainties in the current stress–strain measurements, we will make a simplifying assumption that plastic properties of our samples are isotropic. Under this assumption, we can analyze the results in terms of Levy-von Mises formulation of non-linear rheology, i.e.,

$$\dot{\epsilon}_E = A \sigma_E^n \quad (5)$$

where  $\dot{\epsilon}_E$  and  $\sigma_E$  are the von Mises equivalent strain-rate and stress defined by

$$\dot{\epsilon}_E = \sqrt{\dot{\epsilon}_U^2 + \frac{4}{3}\dot{\epsilon}_S^2} \quad (6)$$

and

$$\sigma_E = \sqrt{\sigma_U^2 + \frac{3}{4}\sigma_S^2} \quad (7)$$

The difference of  $\dot{\epsilon}_S$  due to the geometry is adopted as the uncertainty of  $\dot{\epsilon}_E$  in this study because the difference is larger than that estimated from the uncertainties of  $w$  and  $h$ . This variation in strain-rate causes a variation in stress of ~8% assuming the stress exponent of  $n = 3.5$ .

### 2.3. Microstructures and water content

The microstructures were observed on recovered samples by the secondary electron image (SEI) using field-emission scanning electron microscope (SEM, XL-30 ESEM-FEG). The average grain sizes of the recovered samples (runs #San133 and #D89) and the starting materials were calculated from the SEIs of the samples using the intercept method and a correction factor of the sectioning effect of 1.56 is used.

Dislocations in the recovered samples were observed by the oxidation decoration technique using an SEM (Karato, 1987). Recovered samples were fired at 1073–1103 K in air for 60 min. The dislocations were observed by back-scattered electron image (BSEI) using the SEM.

Water contents in the recovered samples and the starting materials were determined using the FT-IR spectroscopy. The samples were polished at double sides and kept in a vacuum oven at 423 K for more than 12 h before measurements. IR spectra were taken with unpolarized light and an aperture of  $40 \mu\text{m} \times 40 \mu\text{m}$ . Water contents were calculated using a calibration by Paterson (1982) with a density factor for olivine (Kohlstedt et al., 1996).

## 3. Results

The experimental conditions and results are summarized in Table 1. One annealing experiment (run #D89) was conducted at 10 GPa and 1960 K for 60 min to compare the differences of microstructure, grain size and water content between the samples before (after annealing) and after deformation.

### 3.1. Mechanical observations

X-ray diffraction patterns were taken at four different azimuth angles to determine the stresses in the samples (Fig. 5). In this study we used the diffraction from up to six different crystallographic planes. The values of d-spacing of each lattice plane depend on the orientation of each plane with respect to the macroscopic reference frame (i.e., macroscopic stress orientation). We used Eq. (1) to determine stresses and pressure (Fig. 6).

Stress–strain curves are shown in Fig. 7.  $\sigma_S$  reached steady-state at 2–6% equivalent strain at 4.9–9.6 GPa and 1300–1870 K. The stress at steady-state increased with pressure and decreased with temperature (Fig. 7b). Diffraction data from different lattice planes give different stress values (Fig. 7c). The difference in calculated stress is up to a factor of ~3 in these experiments. The stress value calculated from the dislocation density is compared with those calculated from diffraction peaks (1 3 0), (1 1 2), (1 2 2) and (1 4 0) for the run #San133. The X-ray diffraction results give  $\sigma_E$  of 1.7, 1.2,

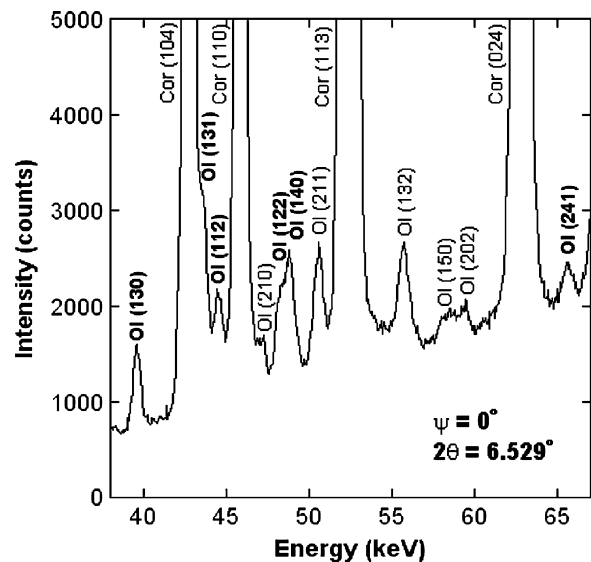


Fig. 5. Representative energy-dispersive X-ray diffraction pattern of olivine collected at  $\psi = 0^\circ$  (vertical diffraction) at 6.2 GPa and 1420 K during annealing (run #San147-1). Olivine (Ol) peaks were observed as well as diffraction peaks from corundum (Cor) pressure medium.



**Table 1**  
Experimental conditions and results

	San133	San132-2	San132-1	San147-3	San147-2	San147-1	D89
Pressure <sup>a</sup> (GPa)	9.6 (1.1)	6.9 (1.0)	8.2 (0.9)	4.9 (0.4)	5.5 (0.6)	6.2 (0.6)	10.0 (1.5)
Temperature <sup>a</sup> (K)	1870 (85)	1630 (85)	1440 (85)	1550 (85)	1420 (85)	1300 (85)	1960 (85)
Equivalent strain rate <sup>a</sup> ( $10^{-5} \text{ s}^{-1}$ )	7.4 (2.6)	0.9 (0.3)	0.6 (0.2)	1.8 (0.6)	2.4 (0.8)	2.2 (0.8)	–
Equivalent strain (%)	45 (16)	11 (4)	8 (3)	10 (3)	8 (3)	12 (4)	–
Equivalent stress <sup>a</sup> (GPa)							
(1 3 0)	1.7 (0.4)	2.3 (0.4)	4.1 (0.4)	1.1 (0.1)	1.8 (0.2)	2.5 (0.2)	–
(1 3 1)	–	–	–	0.5 (0.4)	1.0 (0.3)	1.5 (0.2)	–
(1 1 2)	1.2 (0.3)	1.5 (0.4)	1.3 (0.5)	1.3 (0.3)	1.6 (0.3)	1.6 (0.4)	–
(1 2 2)	0.9 (0.3)	1.2 (0.3)	2.2 (0.4)	1.0 (0.4)	–	1.5 (0.5)	–
(1 4 0)	0.6 (0.3)	1.3 (0.4)	2.3 (0.4)	0.6 (0.4)	–	0.9 (0.3)	–
(2 4 1)	–	–	–	1.2 (0.2)	1.5 (0.3)	2.1 (0.3)	–
Average	1.1 (0.3)	1.6 (0.4)	2.5 (0.4)	1.0 (0.3)	1.5 (0.3)	1.7 (0.3)	–
By dislocation density	1.2 (0.2)	–	–	–	–	–	–
Water content ( $\text{H}/10^6\text{Si}$ )							
Recovered sample	<50	<50	–	<50	–	–	<50
Starting material	2800	2800	2800	1100	1100	1100	2400
Grain size ( $\mu\text{m}$ )							
Recovered sample	5.3 (1.3)	10	–	10	–	–	6.3 (1.7)
Starting material	9.4 (1.3)	9.4 (1.3)	9.4 (1.3)	10.4 (2.0)	10.4 (2.0)	10.4 (2.0)	8.9 (1.3)

The numbers in parenthesis indicate standard deviation.

<sup>a</sup> During steady-state deformation.

0.9, and 0.6 GPa, respectively. The value of deviatoric stress calculated from the dislocation density is  $1.2 \pm 0.2$  GPa which is in good agreement with an average value of stress determined by X-ray diffraction.

The  $\sigma_E$  calculated using different ( $hkl$ ) planes at the steady-state deformations are plotted against  $1/T$  and pressure in Figs. 8 and 9, respectively.  $\sigma_E$  decreases significantly with increasing temperature and increases significantly with pressure. In these plots, data from different pressures are compared after normalization to the same pressure (in Fig. 8) and to the same temperature (in Fig. 9), respectively. The details of the calculations of flow law parameters will be discussed in a later section after the description of microstructures.

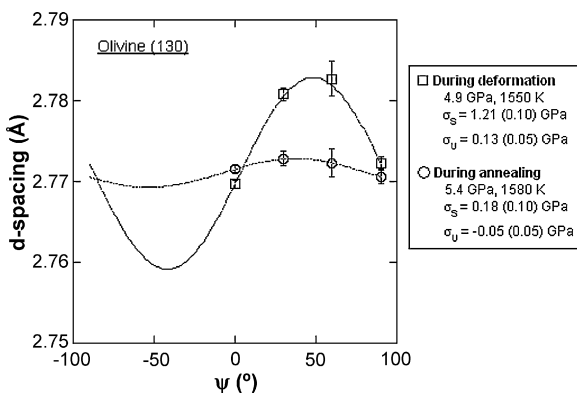
### 3.2. Microstructures and water content

Fig. 4 shows a microstructure of an annealed sample, which would represent the microstructure of a sample before deformation. The average grain-size is  $6.3 \mu\text{m}$ , and grain-boundary

morphology shows nearly equilibrium structure. Dislocations of the annealed sample are shown in Fig. 4b indicating a residual stress of  $\sim 0.1$  GPa.

Microstructures of deformed samples are distinct from those of annealed samples (Fig. 10). Grain-boundaries are serrated and grain-size is reduced. Dislocation density is much higher than that in an annealed sample. However, there are some systematic differences in microstructures of deformed samples that depend on deformation conditions. In the sample deformed at the highest temperature (#San133, deformed at 1870 K and 9.6 GPa), the grain-size is nearly homogeneous but smaller than the starting grain-size. In this sample, many dislocations are curved, and glide loops and numerous subboundaries are observed. These microstructures suggest that deformation in these samples is due to dislocation motion involving both dislocation glide and climb associated with dynamic recrystallization, and the appropriate flow law for such a sample will be a power-law (i.e., Eq. (8)). In contrast, in samples deformed at lower temperatures, grain-size is heterogeneous and much of the regions of samples are occupied by small grains ( $0.9$ – $1.2 \mu\text{m}$ ) suggesting only partial recrystallization. Dislocation structures of these samples (not shown) are characterized by straight dislocations, suggesting that these samples may be deformed in the exponential flow law (the Peierls mechanism) regime where dislocation glide operates with little dislocation climb.

Water contents of deformed samples and starting materials are listed in Table 1 and representative FT-IR spectra are shown in Fig. 1. The water contents in the starting materials ranged from 1100 to  $2800 \text{ H}/10^6 \text{ Si}$  (from 66 to 172 wt. ppm). In the annealing experiment (run #D89), the initial water content in the starting material ( $2400 \text{ H}/10^6 \text{ Si}$ ) was reduced to less than  $50 \text{ H}/10^6 \text{ Si}$  (3 wt. ppm) after annealing, which is comparable with those after deformation (less than  $50 \text{ H}/10^6 \text{ Si}$ ). These results indicate that water contents in the samples were reduced during annealing and the samples were deformed under essentially dry condition (less than  $50 \text{ H}/10^6 \text{ Si}$ ).



**Fig. 6.** Representative d-spacing variation of olivine (1 3 0) with the azimuth angle  $\psi$  during deformation (squares) and annealing (circles) in run #San147-3. Curves are derived by the least-squares fitting of the d-spacings to Eq. (1). Obtained stress values are shown in this figure with experimental conditions. Note that the maximum of the curve during deformation is close to  $45^\circ$ . This means that stress condition in the sample is close to simple shear.

### 3.3. Pressure effect on creep strength: activation volume $V^*$

The extensive study by Evans and Goetze (1979) at 0.1 MPa showed that the flow law of olivine changes from exponential flow law (Peierls mechanism) at high-stresses and low temperatures to

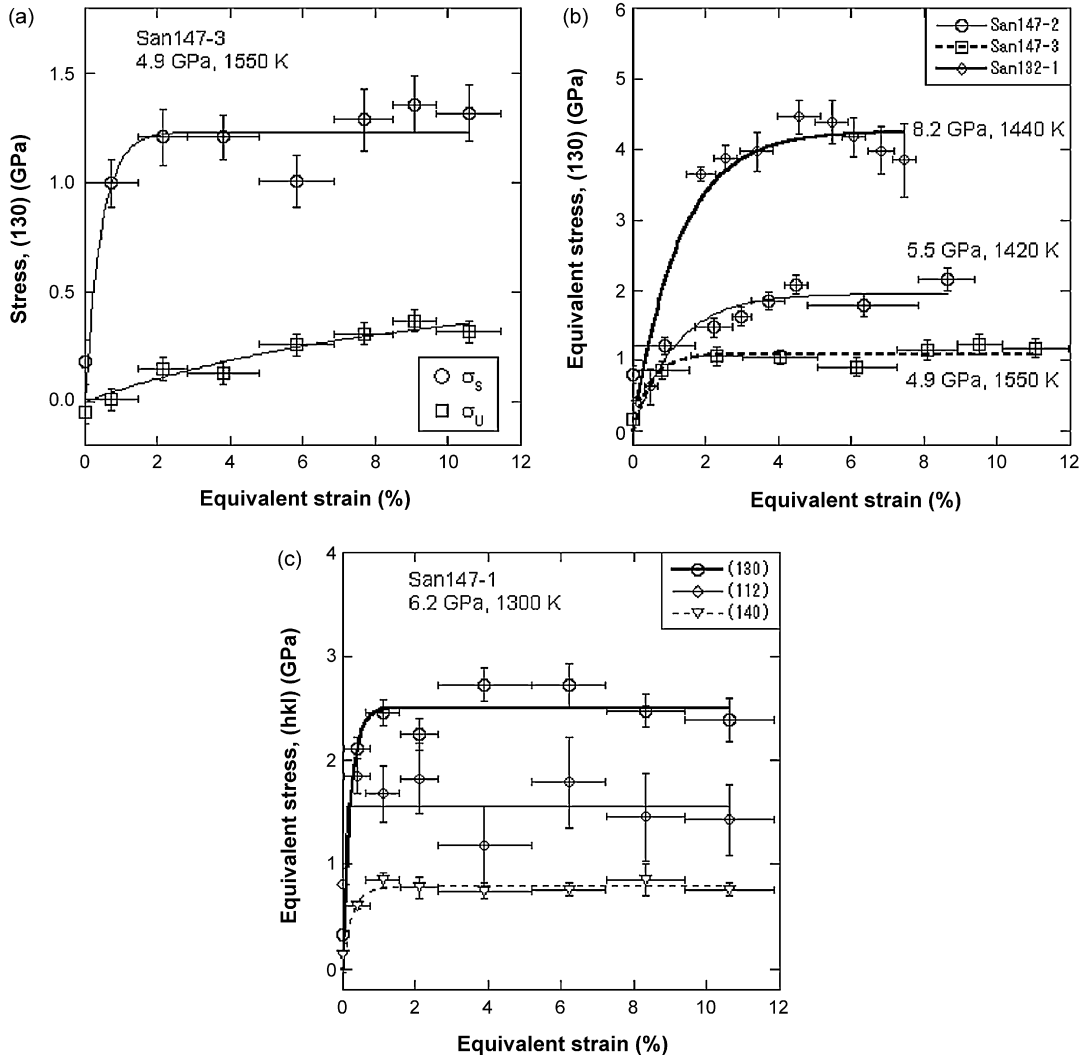


**Fig. 7.** Stress–strain curves. (a) A comparison between shear and uni-axial stresses. Shown are those calculated using (130) plane (run #San147-3). Experimental conditions at steady-state were 4.9 GPa, 1550 K and  $1.8 \times 10^{-5} \text{ s}^{-1}$ . (b) A comparison of stress calculated using the (130) plane between different pressure and temperature conditions. (c) A comparison of stresses calculated using different (hkl) planes (6.2 GPa, 1300 K and  $2.2 \times 10^{-5} \text{ s}^{-1}$ ). Stead-state can be observed from equivalent strain of 1–6%.

power-law at low-stresses and high temperatures. The comparison of our results with these 0.1 MPa results suggests that the experimental conditions in our study likely cover these two rheological regimes (Fig. 11). The microstructural observations presented above also support this notion.

The flow law under the conditions where both dislocation glide and climb are active is the power-law equation, viz.,

$$\dot{\epsilon} = A_{\text{PL}} \sigma^n \exp\left(-\frac{E_{\text{PL}}^* + PV_{\text{PL}}^*}{RT}\right) \quad (8)$$

where  $A_{\text{PL}}$ ,  $E_{\text{PL}}^*$  and  $V_{\text{PL}}^*$  are a pre-exponential constant, the activation energy and the activation volume in the power-law regime, respectively,  $n$  is the stress exponent,  $P$  is the pressure,  $R$  is the gas constant and  $T$  is the temperature. At low temperature, high-stress conditions where only dislocation glide is operative, the following exponential flow law (i.e., the Peierls mechanism) is appropriate,

$$\dot{\epsilon} = A_{\text{PE}} \exp\left[-\frac{E_{\text{PE}}^* + PV_{\text{PE}}^*}{RT} \left(1 - \frac{\sigma}{\sigma_{\text{P}}(P)}\right)^2\right] \quad (9)$$

where  $A_{\text{PE}}$  is a constant,  $\sigma_{\text{P}}$  is the Peierls stress,  $E_{\text{PE}}^*$  is the activation energy, and  $V_{\text{PE}}^*$  is the activation volume in the Peierls regime.

In order to infer the appropriate flow law for our data set, we first plot the strength as a function of temperature (Fig. 8) after normalizing the data to a common pressure (6.9 GPa) and strain-rate ( $10^{-5} \text{ s}^{-1}$ ). This plot indicates that the data from high temperature experiments ( $T > 1550 \text{ K}$ ) show a strong temperature dependence of strength that is consistent with the power-law creep, whereas the data from lower temperatures much weaker temperature sensitivity of strength suggesting an exponential flow law. Consequently, we assume that deformation mechanism at relatively high temperatures and low stresses (runs #San133, #San132-2 and #San147-3) correspond to the power-law creep. Indeed these data fit nicely to Eq. (8) with a reasonable set of parameters, i.e.,  $n = 3.5$  and  $E_{\text{PL}}^* = 530 \text{ kJ/mol}$  (Hirth and Kohlstedt, 2003). Fig. 9 shows the strength as a function of pressure (at a normalized condition of  $T = 1573 \text{ K}$  and strain-rate =  $10^{-5} \text{ s}^{-1}$ ). The data are compared with predicted trends for a range of activation volume,  $V_{\text{PL}}^*$ , assuming the flow law of dry olivine by Hirth and Kohlstedt (2003) at 0.3 GPa. In this plot we also show the data for dry olivine by Mei and Kohlstedt (2000), Jung et al. (2006), Li et al. (2006) and Karato and Rubie (1997). The results show that our data are consistent with  $V_{\text{PL}}^* \sim 15\text{--}20 \times 10^{-6} \text{ m}^3/\text{mol}$  (Table 2) although the uncertainties are difficult to

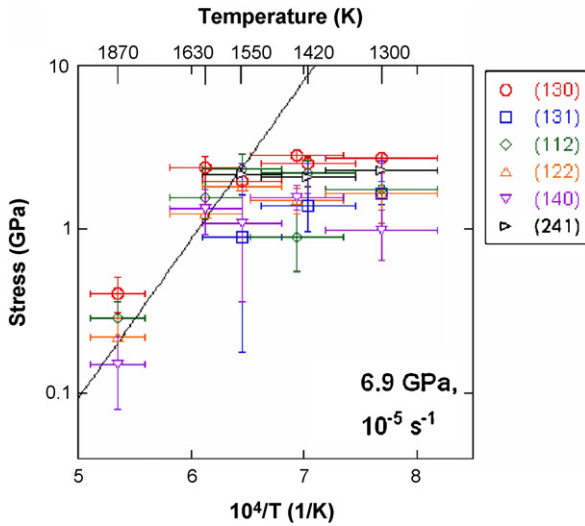


**Fig. 8.** Creep strength as a function of temperature (dry polycrystalline olivine determined for 6.9 GPa and  $10^{-5} \text{ s}^{-1}$ ). Data measured in all runs are normalized to 6.9 GPa and  $10^{-5} \text{ s}^{-1}$  using Eq. (8),  $n=3.5$  (Hirth and Kohlstedt, 2003) and  $V_{PL}^* = 17 \times 10^{-6} \text{ m}^3/\text{mol}$  (this study). Lines in the figures are drawn using Eq. (8) and values listed in Table 2 for power-law creep ( $E_{PL}^* = 530 \text{ kJ/mol}$ ; Hirth and Kohlstedt, 2003).

estimate because of the issues of stress estimates from X-ray diffraction.

For samples deformed at relatively high stresses and low temperatures (runs #San132-2, #San132-1, #San147-3, #San147-2 and #San147-1), the most appropriate flow law is an exponential flow law corresponding to the Peierls mechanism (e.g., Evans and Goetze, 1979). Among these data, runs #San132-2 and #San147-3 are from the intermediate stress and temperature conditions and

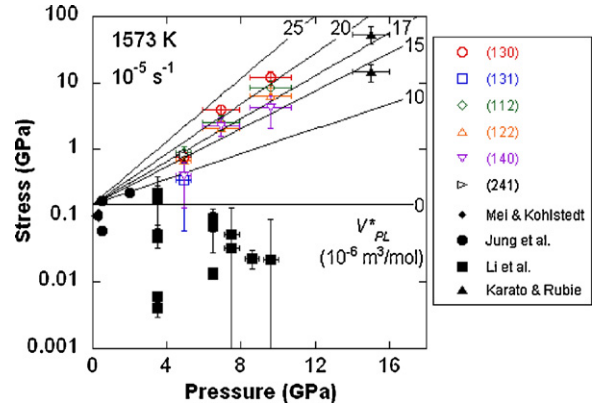


**Fig. 9.** Creep strength as a function of pressure (dry polycrystalline olivine for 1573 K and  $10^{-5} \text{ s}^{-1}$ ). Open symbols indicate stress values determined by each diffraction plane in runs #San147-3, #San132-2 and #San133. Data from Mei and Kohlstedt (2000), Jung et al. (2006), Li et al. (2006) and Karato and Rubie (1997) are also shown as solid diamonds, circles, squares and triangle, respectively. All data are normalized to 1573 K and  $10^{-5} \text{ s}^{-1}$  using Eq. (8),  $n=3.5$  and  $E_{PL}^* = 530 \text{ kJ/mol}$  (Hirth and Kohlstedt, 2003). Straight lines are drawn using Eq. (8), values from Hirth and Kohlstedt (2003) and various activation volumes ( $V_{PL}^* = 0, 10, 15, 17, 20$  and  $25 \times 10^{-6} \text{ m}^3/\text{mol}$ ) for power-law creep.

were included in the analyses both by the power-law creep and the exponential law creep. Eq. (9) is used to analyze these data, in which we assumed the following relationship between the Peierls stress and pressure

$$\sigma_P = \sigma_P^0 \left( 1 + \frac{G'P}{G_0} \right) \quad (10)$$

where  $\sigma_P^0$  is the Peierls stress at ambient pressure,  $G_0$  is the shear modulus at ambient pressure and  $G'$  is its pressure derivative (Liu et

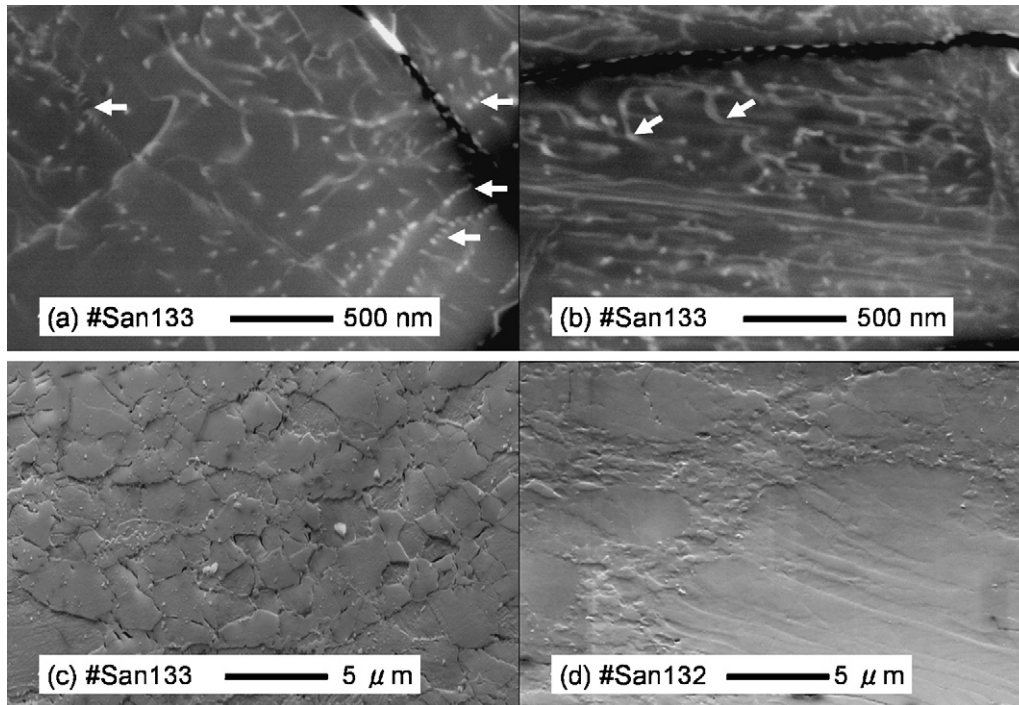


**Fig. 10.** Microstructures of recovered samples. (a) and (b) Dislocation structures of a sample deformed to the equivalent strain of 45% at 1870 K, 9.6 GPa and  $7.4 \times 10^{-5} \text{ s}^{-1}$  (run #San133) observed by back-scattered electron imaging. Arrows indicate subboundaries and glide loops in (a) and (b), respectively. (c) SEI of the sample of run #San133. (d) SEI of a sample deformed at 6.9–8.2 GPa, 1440–1630 K and  $0.6\text{--}0.9 \times 10^{-5} \text{ s}^{-1}$  (run #San132). Bimodal grain sizes are observed as a result of partial dynamic recrystallization. The samples were sectioned in X–Z plane and etched using 35%  $\text{HNO}_3$  in (c) and (d). The shear (X) direction is horizontal in these figures.

**Table 2**  
Rheological parameters of dislocation creep

	$A^a$ ( $s^{-1} MPa^{-1}$ )	$n$	$E^*$ (kJ/mol)	$V^*$ ( $10^{-6} m^3/mol$ )	$\sigma_p^0$ (GPa)
<b>Power-law regime</b>					
This study	$10^{5.04}$ <sup>b</sup>	3.5 <sup>b</sup>	530 <sup>b</sup>	15–20	–
Li et al. (2006)	–	3	470	0 ± 5	–
Hirth and Kohlstedt (2003)	$10^{5.04}$	$3.5 \pm 0.3$	$530 \pm 4$	–	–
Karato and Jung (2003)	$10^{6.1 \pm 0.2}$	$3.0 \pm 0.1^c$	$510 \pm 30^c$	$-14 \pm 2$	–
Green and Borch (1987)	–	–	–	27	–
<b>Peierls regime</b>					
This study	$10^{12.1d}$	–	502 <sup>d</sup>	~30	9.1 <sup>d</sup>
Evans and Goetze (1979)	$10^{12.1 \pm 0.5}$	–	$502 \pm 126$	–	$9.1 \pm 0.1$

<sup>a</sup> Stress in MPa.

<sup>b</sup> From Hirth and Kohlstedt (2003).

<sup>c</sup> From Mei and Kohlstedt (2000).

<sup>d</sup> From Evans and Goetze (1979).

al., 2005). The data are compared with predicted trend for an activation volume,  $V_{PE}^*$ , assuming the flow law of dry olivine by Evans and Goetze (1979) at 0.1 MPa (Fig. 11). As a result, our data are consistent with  $V_{PE}^* \sim 30 \times 10^{-6} m^3/mol$  (Table 2).

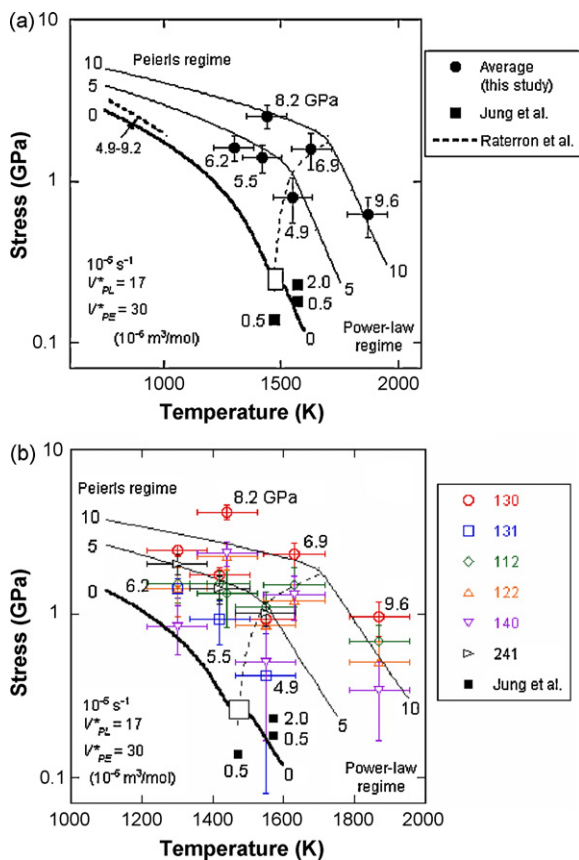


**Fig. 11.** Relationship between stress, temperature and pressure for the strain rate of  $10^{-5} s^{-1}$ . Average stress and stresses calculated using different  $(hkl)$  planes are shown in (a) and (b), respectively, with data of Jung et al. (2006) and Raterron et al. (2004). The strain rates of all data are normalized to  $10^{-5} s^{-1}$ . Pressure values are shown as numbers near symbols and lines in GPa. A bold line is the relationship for Peierls and power-law regimes at 0 GPa from Evans and Goetze (1979) and Hirth and Kohlstedt (2003), respectively. White box indicates the transition region from Peierls mechanism to power-law determined at ambient pressure (Evans and Goetze, 1979). Thin lines are relationships at 5 and 10 GPa and dashed line is transition region, estimated for values listed in Table 2 ( $V_{PL}^* = 17$  and  $V_{PE}^* = 30 \times 10^{-6} m^3/mol$ ).

#### 4. Discussion

The results of this study are compared with other data in Fig. 9 as a function of pressure. Creep strength of dry polycrystalline olivine studied here significantly increased with increasing pressure. Our data are also consistent with the previous results at lower pressures (Mei and Kohlstedt, 2000; Jung et al., 2006). Our results are also compared with the results by Karato and Rubie (1997) from the stress relaxation tests ( $V_{PL}^* = 14 \times 10^{-6} m^3/mol$  for  $n=3$ ,  $V_{PL}^* = 18 \times 10^{-6} m^3/mol$  for  $n=5$ ). These data sets can be interpreted by a power-law creep formula with the activation volume of  $\sim 15\text{--}20 \times 10^{-6} m^3/mol$ .

However, our results are in marked contrast with those by Li et al. (2006) (similar results were also published by Li et al. (2003, 2004)) using a D-DIA which showed that the strength of olivine does not change with pressure so much (in fact their data show that the strength decreases with pressure). The reason for the large discrepancy is not known but may include: (i) a higher water content (some of their samples have water contents up to 235 wt. ppm), (ii) the influence of transient creep (most of the strength data were taken at low strains and the achievement of “steady-state” was not confirmed in these studies), and (ii) the influence of fine-grained materials (they used powder samples as starting materials and the degree of annealing was not clearly documented).

Green and Borch (1987) reported a higher activation volume but later studies Young et al. (1993) indicated that their sample contained a large amount of water (see a discussion by Hirth and Kohlstedt (1996)). Consequently, their data cannot be compared to our data on dry olivine.

The pressure dependence of creep under water-saturated conditions includes the pressure dependence of solubility as well as the pressure dependence of defect (dislocation) mobility (e.g., Karato, 2008). Karato and Jung (2003) determined that  $V_{PL}^* = 24 \times 10^{-6} m^3/mol$  for water-saturated conditions, and interpreted that this activation volume includes the activation volume for water dissolution ( $\sim 10 \times 10^{-6} m^3/mol$ ; Kohlstedt et al., 1996) and that for dislocation motion ( $\sim 14 \times 10^{-6} m^3/mol$ ). The present result of  $V_{PL}^* = 15\text{--}20 \times 10^{-6} m^3/mol$  may be compared with  $V_{PL}^* = 14 \times 10^{-6} m^3/mol$  for dislocation mobility under wet conditions. A small difference in  $V_{PL}^*$  ( $14 \times 10^{-6} m^3/mol$  for wet conditions,  $V_{PL}^* = 15\text{--}20 \times 10^{-6} m^3/mol$  for dry conditions) is consistent with a general trend that shows a correlation between the activation energy and activation volume (see Karato, 2008), but it may reflect a subtle difference in the microscopic mechanisms dislocation motion under these conditions such as the difference in the kinetics of dis-



**Table 3**

Recommended flow law parameters for power-law dislocation creep in olivine aggregates for an open system:  $\dot{\epsilon} = A_d \sigma^{n_d} \exp(-(E_d^* + PV_d^*)/RT) + A_w \sigma^{n_w} \exp(-(E_w^* + PV_w^*)/RT)$ , and for a closed system:  $\dot{\epsilon} = A_d \sigma^{n_d} \exp(-(E_d^* + PV_d^*)/RT) + A_w C_{OH} \sigma^{n_w} \exp(-(E_w^* + PV_w^*)/RT)$

Parameter	Value	Source
$V_d^*$	$17 \times 10^{-6} \text{ m}^3/\text{mol}$	This study
$V_w^*$	$24 \pm 3 \times 10^{-6} \text{ m}^3/\text{mol}$	Karato and Jung (2003)
$V_w^{*c}$	$11 \pm 3 \times 10^{-6} \text{ m}^3/\text{mol}$	Karato and Jung (2003)
$A_d$	$10^{5.04} \text{ s}^{-1} \text{ MPa}^{-n}$	Hirth and Kohlstedt (2003)
$A_w$	$10^{2.9 \pm 0.1} \text{ s}^{-1} \text{ MPa}^{-n-r}$	Karato and Jung (2003)
$A_w^c$	$10^{0.56 \pm 0.02} \text{ s}^{-1} \text{ MPa}^{-n}$	Karato and Jung (2003)
$r$	$1.20 \pm 0.05$	Karato and Jung (2003)
$E_d^*$	$530 \pm 4 \text{ kJ/mol}$	Hirth and Kohlstedt (2003)
$E_w^*$	$470 \pm 40 \text{ kJ/mol}$	Mei and Kohlstedt (2000)
$E_w^{*c}$	$410 \pm 40 \text{ kJ/mol}$	Karato and Jung (2003)
$n_d$	$3.5 \pm 0.3$	Hirth and Kohlstedt (2003)
$n_w$	$3.0 \pm 0.1$	Mei and Kohlstedt (2000)

location climb or glide (or the differences in the rate-controlling slip system(s)). Table 3 summarize the recommended flow law parameters for power-law dislocation creep in olivine based on the present study and Karato and Jung (2003).

## 5. Summary

We have presented the first quantitative results on deformation of dry olivine aggregates (water content less than 50H/10<sup>6</sup> Si) to pressure of 9.6 GPa and temperature of 1870 K (at strain-rate  $\sim 10^{-5} \text{ s}^{-1}$ ) to large strains. Flow laws at “steady-state” are examined based on the stress and strain-rates determined by the synchrotron in situ X-ray observations. We infer, based on the mechanical data and microstructural observations, that either power-law or exponential creep (the Peierls mechanism) operates in these samples depending on the temperature. In both regimes, the influence of pressure is large. The results for the power-law creep can be interpreted by an activation volume of  $\sim 15\text{--}20 \times 10^{-6} \text{ m}^3/\text{mol}$ . As we will discuss below, there still are a number of technical issues particularly regarding the use of X-ray diffraction to estimate the sample stress. Nevertheless, when dislocation density is also used, the uncertainties in stress measurements are less than  $\sim 20\%$ . Given the fact that these measurements of flow properties were made at nearly the same conditions in the deep upper mantle in the power-law creep regime, we consider that the present results provide robust estimates of the creep strength of the deep upper mantle. Combining the results by Karato and Jung (2003) on wet olivine, we present recommended parameters for dislocation creep in olivine for both wet and dry conditions (Table 3).

Although these results provide the first experimental constraints on olivine flow law that can be applied to deep upper mantle dynamics, we also recognize a number of technical issues. First, the theory for stress estimate from X-ray diffraction needs to be developed. The currently used theory by Singh (1993) cannot explain the observed large variation in stress values from different diffraction planes. Second, the present results are for dry olivine. The influence of water on deformation is large (e.g., Mei and Kohlstedt, 2000; Karato and Jung, 2003) and needs to be characterized under deep upper mantle conditions (Karato and Jung (2003)'s work was up to 2.2 GPa). Third, the present results are for dislocation creep. Bejina et al. (1999) reported the small pressure effects on Si diffusion in olivine. If such results are applicable to upper mantle, it would imply a dominant role of diffusion creep in the deep upper mantle (e.g., Karato and Wu, 1993). However,

the influence of pressure on diffusion and diffusion creep has not been investigated in any detail. Further progress in these areas are essential to improve our understanding of mantle dynamics based on mineral physics studies.

## Acknowledgements

This study has been supported by Consortium for Materials Properties Research in Earth Sciences (COMPRES) and by grants from National Science Foundation. We appreciate supports by L. Wang, M. Vaughn, and C. Koleda, and D.J. Weidner for synchrotron experiments.

## References

- Bejina, F., Jaoul, O., Liebermann, R.C., 1999. Activation volume of Si diffusion in San Carlos olivine: implications for upper mantle rheology. *J. Geophys. Res.* 104, 25529–25542.
- Chen, J., Li, L., Weidner, D., Vaughan, M., 2004. Deformation experiments using synchrotron X-rays: in situ stress and strain measurements at high pressure and temperature. *Phys. Earth Planet. Int.* 143/144, 347–356.
- Evans, B., Goetze, C., 1979. The temperature variation of hardness of olivine and its implication for polycrystalline yield stress. *J. Geophys. Res.* 84, 5505–5524.
- Gasparik, T., 1996. Melting experiments on the enstatite-diopside join at 70–224 kbar, including the melting of diopside. *Contrib. Miner. Petrol.* 124, 139–153.
- Green II, H.W., Borch, R.S., 1987. The pressure dependence of creep. *Acta Metall.* 35, 1301–1305.
- Hirth, G., Kohlstedt, D.L., 1996. Water in the oceanic upper mantle: implications for rheology, melt extraction and the evolution of the lithosphere. *Earth Planet. Sci. Lett.* 144, 93–108.
- Hirth, G., Kohlstedt, D., 2003. Rheology of the upper mantle and the mantle wedge: a view from the experimentalists. In: Eiler, J. (Ed.), *Inside the Subduction Factory*. Am. Geophys. Union, Geophys. Monogr. Ser. 138, pp. 83–105.
- Jung, H., Katayama, I., Jiang, Z., Hiraga, T., Karato, S., 2006. Effect of water and stress on the lattice-preferred orientation of olivine. *Tectonophysics* 421, 1–22.
- Karato, S., 1987. Scanning electron microscope observation of dislocation in olivine. *Phys. Chem. Miner.* 14, 245–248.
- Karato, S., 2008. *Deformation of Earth Materials: Introduction to the Rheology of the Solid Earth*. Cambridge University Press, Cambridge.
- Karato, S., Jung, H., 2003. Effects of pressure on high-temperature dislocation creep in olivine. *Philos. Mag.* 83, 401–414.
- Karato, S., Rubie, D.C., 1997. Toward an experimental study of deep mantle rheology: a new multianvil sample assembly for deformation studies under high pressures and temperatures. *J. Geophys. Res.* 102, 20111–20122.
- Karato, S., Wu, P., 1993. Rheology of the upper mantle: a synthesis. *Science* 260, 771–778.
- Kohlstedt, D.L., Keppler, H., Rubie, D.C., 1996. Solubility of water in the  $\alpha$ ,  $\beta$  and  $\gamma$  phases of  $(\text{Mg}, \text{Fe})_2\text{SiO}_4$ . *Contrib. Miner. Petrol.* 123, 345–357.
- Li, L., Raterron, P., Weidner, D.J., Chen, J., 2003. Olivine flow mechanisms at 8 GPa. *Phys. Earth Planet. Int.* 138, 113–129.
- Li, L., Weidner, D., Raterron, P., Chen, J., Vaughan, M., 2004. Stress measurements of deforming olivine at high pressure. *Phys. Earth Planet. Int.* 143/144, 357–367.
- Li, L., Weidner, D., Raterron, P., Chen, J., Vaughan, M., Mei, S., Durham, B., 2006. Deformation of olivine at mantle pressure using the D-DIA. *Eur. J. Miner.* 18, 7–19.
- Liu, W., Kung, J., Li, B., 2005. Elasticity of San Carlos olivine to 8 GPa and 1073 K. *Geophys. Res. Lett.* 32, L16301.
- Liu, W., Li, B., 2006. Thermal equation of state of  $(\text{Mg}_{0.9}\text{Fe}_{0.1})_2\text{SiO}_4$  olivine. *Phys. Earth Planet. Int.* 157, 188–195.
- Mei, S., Kohlstedt, D.L., 2000. Influence of water on plastic deformation of olivine aggregates. 2. Dislocation creep regime. *J. Geophys. Res.* 105, 21471–21481.
- Paterson, M.S., 1982. The determination of hydroxyl by infrared absorption in quartz, silicate glasses and similar materials. *Bull. Miner.* 105, 20–29.
- Raterron, P., Chen, J., Li, L., Weidner, D.J., Cordier, P., 2007. Pressure-induced slip system transition in forsterite: single-crystal rheological properties at mantle pressure and temperature. *Am. Miner.* 92, 1436–1445.
- Raterron, P., Wu, Y., Weidner, D.J., Chen, J., 2004. Low-temperature olivine rheology at high pressure. *Phys. Earth Planet. Int.* 145, 149–159.
- Singh, A.K., 1993. The lattice strain in a specimen (cubic system) compressed nonhydrostatically in an opposed anvil device. *J. Appl. Phys.* 73, 4278–4286.
- Wang, Y., Durham, W.B., Getting, I.C., Weidner, D.J., 2003. The deformation-DIA: a new apparatus for high temperature triaxial deformation to pressures up to 15 GPa. *Rev. Sci. Instrum.* 74, 3002–3011.
- Weidner, D.J., Li, L., Davis, M., Chen, J., 2004. Effect of plasticity on elastic modulus measurements. *Geophys. Res. Lett.* 31, doi:10.1029/2003GL019090.

- Xu, Y., Nishihara, Y., Karato, S., 2005. Development of a rotational Drickamer apparatus for large-strain deformation experiments at deep Earth conditions. In: Chen, J.M., Wang, Y., Duffy, T.S., Shen, G., Dobrzhinetskaya, L.F. (Eds.), *Advance in High-Pressure Technology for Geophysical Applications*. Elsevier, pp. 167–182.
- Yamazaki, D., Karato, S., 2001. High-pressure rotational deformation apparatus to 15 GPa. *Rev. Sci. Instrum.* 72, 4207–4211.
- Young, T.E., Green II, H.W., Hofmeister, A.M., Walker, D., 1993. Infrared spectroscopic investigation of hydroxyl in  $\beta$ -(Mg,Fe)<sub>2</sub>SiO<sub>4</sub> and coexisting olivine: implications for mantle evolution and dynamics. *Phys. Chem. Miner.* 19, 409–422.